Journal of Chromatography A, 1218 (2011) 5401–5413

Contents lists available at ScienceDirect

Journal of Chromatography A

journal homepage: www.elsevier.com/locate/chroma

Influence of physical properties and operating parameters on hydrodynamics in Centrifugal Partition Chromatography☆

S. Adelmann, G. Schembecker*

Laboratory of Plant and Process Design, Department of Biochemical and Chemical Engineering, Technische Universität Dortmund, D-44221 Dortmund, Germany

ARTICLE INFO

Article history:
Received 12 October 2010
Received in revised form 19 January 2011
Accepted 21 January 2011
Available online 27 January 2011

Keywords:
Flow pattern, CPC, Hydrodynamics, Coriolis force, Retention, Physical properties, Visualization, Image processing

ABSTRACT

Besides the selection of a suitable biphasic solvent system the separation efficiency in Centrifugal Partition Chromatography (CPC) is mainly influenced by the hydrodynamics in the chambers. The flow pattern, the stationary phase retention and the interfacial area for mass transfer strongly depend on physical properties of the solvent system and operating parameters. In order to measure these parameters we visualized the hydrodynamics in a FCPC®-chamber for five different solvent systems with an optical measurement system and calculated the stationary phase retention, interfacial area and the distribution of mobile phase thickness in the chamber. Although inclined chambers were used we found that the Coriolis force always deflected the mobile phase towards the chamber wall reducing the interfacial area. This effect increased for systems with low density difference. We also have shown that the stability of phase systems (stationary phase retention) and its tendency to disperse increased for smaller values of the ratio of interfacial tension and density difference. But also the viscosity ratio and the flow pattern itself had a significant effect on retention and dispersion of the mobile phase. As a result operating parameters should be chosen carefully with respect to physical properties for a CPC system. In order to reduce the effect of the Coriolis force CPC devices with greater rotor radius are desirable.

1. Introduction

Centrifugal Partition Chromatography (CPC) is one form of liquid–liquid chromatography. The separation is based on the partition of components in the two phases of an immiscible liquid system. The stationary phase, that can be the lower or upper one, is retained in the chambers of the rotating CPC rotor by centrifugal force and the mobile phase is pumped through the stationary one [1].

A CPC device contains chambers that are connected by ducts in a cascade. In commercially available rotors several hundred or more chambers are connected. In contrast to hydrodynamic Counter Current Chromatography (CCC) [2], which works with coiled tubing, in CPC the chambers rotate around a single axis and create a uniform centrifugal field. Therefore it is also called hydrostatic CCC although the abbreviation CPC should be used. The flow rate and rotational speed of the rotor are limited by the maximum working pressure of the rotary joints.

The separation efficiency in CPC is affected by a variety of parameters that can be classified in three different groups. The first group of parameters depends on the sample properties in the solvent system. In order to separate the target component(s) it should have a suitable distribution ratio K_D in the range between 0.25 and 16 [3] that differs from the distribution ratio of the impurities to have an adequate selectivity factor. Besides these two necessary conditions also the sample solubility belongs to the first group. Good solubility enhances mass transfer between both phases, increases the productivity and thus belongs to the sufficient conditions for a good separation.

The second and third groups are physical properties of the solvent system (interfacial tension, densities, viscosities) and the operating parameters (volume flow, rotational speed, chamber geometry, mode of operation, injection volume, sample concentration). The parameters of both groups belong to the sufficient conditions for a good separation and most of those affect the hydrodynamics in the chambers. Especially the hydrodynamics (degree of dispersion, interfacial area for mass transfer, the stationary phase retention) have major influence on resolution and thus on separation efficiency.

The influence of hydrodynamics in CPC was already analyzed by several authors. In 1994 Foucault [4] introduced the Stokes Model to describe the influence of physical properties in CPC and classified the stability of solvent systems dependent on the stationary phase retention. He proved that stationary phase retention is strongly dependent on the ratio of interfacial tension and density difference. Additionally he found for the Sanki HPCPC that he used that the separation efficiency in a heptane/methanol biphasic system increased for higher centrifugal force due to greater dispersion of

☆ Presented at the 13th Symposium on Preparative and Industrial Chromatography and Allied Techniques, Stockholm, Sweden, 12–15 September 2010.

* Corresponding author.
E-mail address: gerhard.schembecker@bci.tu-dortmund.de (G. Schembecker).

0021-9673/$ – see front matter © 2011 Elsevier B.V. All rights reserved.
doi:10.1016/j.chroma.2011.01.064

Nomenclature

a, b	coefficients of regression functions
c	concentration
Ca_{crit}	critical capillary number
ch	chamber
d	diameter, thickness
E	extinction
f	unknown function, frequency
I	light intensity
P	pixel
Sf	stationary phase volume retention factor/retention
R	distance to rotation axis
$\vec{S}$	(x,y,z) vector
$\vec{x}$, $\vec{y}$	arrays used for curve fits

Greek symbols

ε	extinction coefficient
η	dynamic viscosity
$\dot{\gamma}$	shear rate
ρ	density
σ	interfacial tension
ω	angular velocity

Abbreviations

MB	methylene blue
LED	light emitting diode
GV	grey scale value
FCPC®	Fast Centrifugal Partition Chromatography
CCD	charge coupled device

Subscripts

blank	from a blank image
c	continuous
cal	in the calibration
d	droplet, disperse
duct	of the duct
flow	from a flow image
i	control variable
lp	lower phase
m	mobile phase
max	maximum
mean	mean value
rad	radial component
retention	from a retention image
rot	rotor
s	stationary phase
tan	tangential component
up	upper phase
xy	coordinates of an image
0,1,2	specific state
0,1,2,3,4	specific pixel position
λ	for a specific wavelength

the mobile phase. Foucault also suggested that flow visualization would help to understand the phenomena.

van Buel [5] was the first to visualize the two phase flow in the chambers of a CPC device and discovered the different flow patterns in CPC chambers. He also proved the dependence of separation efficiency on volume flow and rotational speed. With a model for the effluent concentration profile he calculated the relative contribution of axial dispersion of the mobile phase, off-column mixing and mass transfer limitations [6].

The next big step in understanding the flow phenomena and improving the separation efficiency of CPC devices was done by Marchal [7]. He visualized the flow in a "Visual-CPC"-rotor from a different position compared to van Buel and found a strong effect of the Coriolis force on the flow pattern. These results helped to design different chamber geometries with respect to the Coriolis force that were patented during the last ten years (FCPC®-chamber [8], Twin Cells [9], Asymmetric Twin Cells [10]). These chambers improve dispersion of the mobile phase for enhanced mass transfer and provide a higher stationary phase retention.

The liquid stationary phase offers another possibility for improving the separation efficiency. As the flow direction can be changed at any time different modes of operation were developed in addition to the classical elution in descending (lower phase is mobile) or ascending (upper phase is mobile) mode. Examples are dual-mode with single, repeated [11] and continuous [12] sample injection, elution–extrusion [13] and elution-back extrusion [14] mode. But the general hydrodynamics stay the same as in the classical descending or ascending mode. The only difference for dual-mode operation is the desired stationary phase retention close to 50% and not "as high as possible".

For optimization of the injection step Marchal [15] performed experiments on flooding conditions to get the maximum allowed sample concentration that changes the sample density. Surfactants and the direction of mass transfer, that alter the interfacial tension and hence dispersion and coalescence, were not investigated in CPC yet. Although the physical properties are known to have a great impact on the separation, their influence on the hydrodynamics are hardly predictable and still unclear. The stationary phase retention was measured for some CPC instruments [16,17] but the degree of dispersion and the interfacial area for mass transfer were not accessible quantitatively. Additionally the selection of suitable operating parameters for given physical properties still depends on the experience of the chromatographer and the pressure limit of the rotary joints.

In this study we want to focus on the effect of volume flow and rotational speed on the hydrodynamics for different phase systems. For investigation of the multiphase flow pattern we designed an optical measurement system that is described in Section 2.1. The hydrodynamics of five different aqueous organic solvent systems with different physical properties were visualized in a FCPC®-chamber of a wide range of volume flow and rotational speed. From the images the stationary phase retention, the interfacial area and the mobile phase thicknesses distribution in the chamber were calculated by an implemented image processing routine in ImageJ [18] (see Section 3).

2. Materials and methods

2.1. Optical measurement system

The set-up of the optical measurement system is shown schematically in Fig. 1. From a tempered reservoir the solvent was pumped into the CPC device (FCPC® Semi Preparative, KROMATON) that was equipped with a self-made transparent rotor. The UV-detector (ProStar 325 UV-Vis Detector, VERIAN) was used for detection of the hydrodynamic equilibrium and a 40 psi (2.75 bar) pressure reducer was used to operate the detector at enhanced pressure. The signal became smooth when there was no more carry-over of stationary phase. From the UV-detector the solvent could be recycled into the reservoir or disposed of into a waste container.

2.1.1. Transparent rotor

The transparent rotor consisted of a single FCPC® plate that contained 66 chambers connected by ducts with an internal volume of 10 ml (according to the manufacturer) and is shown in

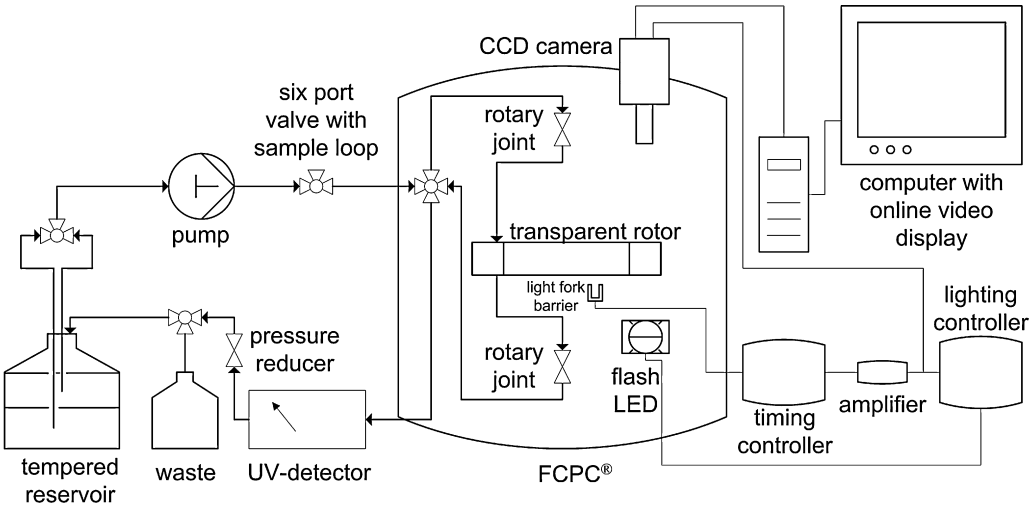

Fig. 1. Schematic set-up of optical measurement system with video instrumentation.

Fig. 2. The plate had a height of 2.5 mm, the ducts were approximately 0.35 mm wide and the inclined chambers were about 4.4 mm × 11 mm × 2.5 mm. The rotor had an outer diameter of 250 mm and the middle of each chamber had a rotational radius of 105.15 mm that resulted in a centrifugal acceleration between 415 m/s^2 (600 rev/min) and 3736 m/s^2 (1800 rev/min).

On top and bottom of the rotor plate there was first a glass sheet and then a specially designed aluminum plate with five symmetrically placed viewing ports. The whole assembly was tightened with 48 screws as shown in Fig. 2. For sealing purposes two transparent sheets of 127 μm FEP-foil (fluorinated ethylene propylene) were placed between the rotor plate and glass plates on each side. In order to compensate unevenness of the aluminum plates an extra sheet of FEP-foil was used between the aluminum and glass plates. The problem of a tight connection of HPLC tubing and inlet and outlet of the rotor plate was solved by using self-made connectors with a M10 thread on the outside that could be tightened into the aluminum plate. At these connection positions additional holes with a diameter of 8 mm were drilled into the glass plates. The sealing was done by tightening the connectors onto the FEP-foil and rotor plate with PTFE (poly tetra fluor ethylene) rings in between. Each PTFE ring has an outer diameter of 7.9 mm, a thickness of 2 mm and a 1.5 mm hole. The hole was also pierced into the two FEP-foils on the top of the rotor. Both connections were on the top of the rotor because of easier assembly. The regular HPLC tubing from or to the rotary joints was screwed into the internal N10-32 UNF thread of the connectors. The transparent rotor showed absolutely no leakage for back pressures up to 20 bar. The special feature was the possibility of transmitted light illumination and the use of transparent foils.

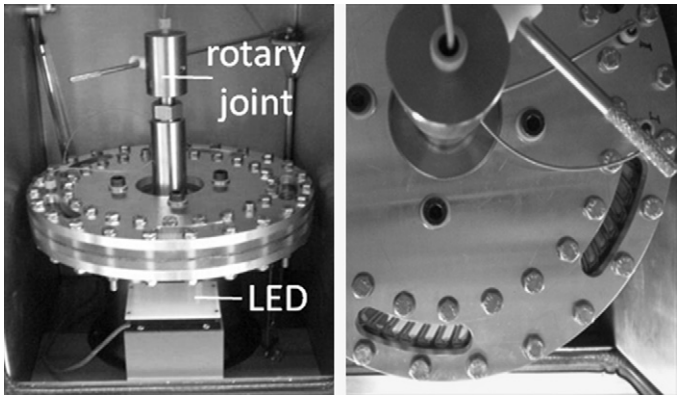

Fig. 2. Transparent rotor used for flow visualization.

2.1.2. Video instrumentation

For grabbing flow videos of the chambers the FCPC® was equipped with a monochrome CCD-camera (AccuPIXEL® TM 1327GE, JAI PULNIX). The camera was able to take 8-bit grey scale images with a resolution of 1392 × 1040 pixels and a maximum frequency of 30 Hz. The illumination was achieved using a red flash-LED (CCS LD-TP/LDL Series, STEMMER IMAGING) with a wavelength of 630 ± 7 nm. A small metal plate was fixed to one screw on the lower side of the rotor that triggered a light fork barrier one time per rotation. This signal was transmitted to a timing controller (Gard 320CC, GARDASOFT VISION) and converted into a 10 ms digital 5 V trigger pulse by an amplifier. From the amplifier the trigger signal was transmitted to the camera and to the lighting controller (Gard 420F, GARDASOFT VISION) that allowed shifting the trigger signal and flash times of the LED from 1 μs to continuous illumination. In the used range of illumination time (below 10 μs) the LED could be charged with a tenfold higher current compared to the maximum allowed current for continuous illumination. As the minimum shutter speed of the camera was 63.5 μs and the illumination time of the LED was below 10 μs, the overall exposure time (time the CCD sensor is exposed to the highlighted source) is only set by the LED.

In order to take one image per rotation of the same chamber position the delay time of the LED illumination was manually adjusted in the lighting controller (420F) for each rotational speed of the rotor. The exposure time of the camera was set to a constant value. The time between LED pulse and closing the shutter and reading out the charge should be as short as possible (see Fig. 3) to avoid inaccuracies because of charge diffusion or scattered radiation. The

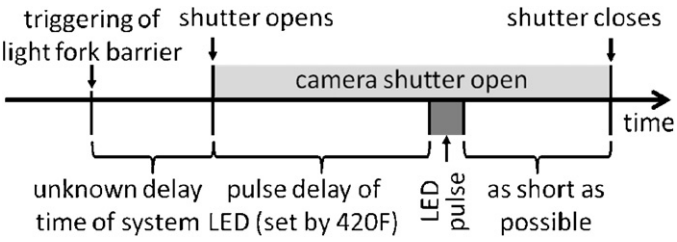

Fig. 3. Timing control of flash LED and camera shutter (times not to scale).

Table 1
Solvent systems and their physical properties (EtAc: ethyl acetate, Wat: water, Hep: n-heptane, MeOH: methanol, ACN: acetonitrile, EtOH: ethanol).

Solvents	EtAc.Wat	Hep, EtAc, MeOH.Wat	Hep, EtAc, ACN,Wat	Hep.EtOH, Wat	Hep, EtAc, MeOH,Wat
Abbreviation of solvent system used	EtAcWat	7:3:6:5	ACN	EtOH	6:4:5:5
Composition (by volume)	1:1	7:3:6:5	71:8:50:71	4:4:1	6:4:5:5
Density ρ_{up} [kg/m^3]	892.8	709.3	688.2	682.2	769.5
Density ρ_{ip} [kg/m^3]	996.3	915.1	926.7	837.4	923.9
Density difference $\Delta\rho$ [kg/m^3]	103.5	205.8	238.5	155.2	154.4
Interfacial tension σ [mN/m]	6.45	5.9	6.35	3.1	2.2
Dyn. viscosity η_{up}[mPa s]	0.47	0.38	0.38	0.40	0.40
Dyn. viscosity η_{ip} [mPa s]	1.07	1.45	0,91	1.78	1.44
Parameter $\sigma/\Delta\rho$ [s^2/cm^3]	62.0	28.6	26.6	20.0	14.3

elapsed time between opening the shutter of the camera and the same chamber position had a maximum for the smallest rotational speed. Therefore the shutter time of the camera was adjusted to a constant value of 3000 μs that still allowed taking images of the lowest rotational speed.

2.2. Chemicals

Ethanol (99.9%) and methanol (99.8%) were purchased from VWR International. Ethyl acetate (99.9%) and n-heptane (>99%) were from Carl Roth GmbH + Co KG, acetonitrile was from Fisher Scientific and the water was demineralized. The water free polar dye methylene blue (dye content > 82%) was from Merck KGaA.

2.3. Experimental procedures

For flow visualization five different solvent systems were selected and their physical properties measured (see Table 1). The ethyl acetate/water (EtAcWat) system was selected because it is a very stable system [4] that already was visualized in CPC [5]. The n-heptane/ethyl acetate/methanol/water systems (7:3:6:5 and 4:6:5:5) belong to the commonly used ARIZONA system that was introduced by Margraff [19] (the composition of the 7:3:6:5 system is not listed in the original ARIZONA solvent system). The n-heptane/ethanol/water (EtOH) system was selected because ethanol is often used as extraction solvent, is permitted for all food applications and has no limitation in foodstuffs, unlike methanol, for example, which is limited to 1.5 mg/kg [20]. The fifth system investigated (ACN) containing acetonitrile was found in a previous work to give suitable distribution ratios for the separation of specific secondary metabolites. The system was developed because some metabolites tend to denaturize in the presence of alcohols (especially in methanol). The hydrodynamics of all solvent systems were measured in descending mode (lower phase mobile) for volume flows from 3 to 30 ml/min and rotational speeds between 600 and 1800 rev/min.

2.3.1. Setting up the solvent systems

The solvent systems were prepared by mixing all solvents and shaking vigorously. The systems were equilibrated at 25 °C over night. For the hydrodynamic experiments 500 ml of lower phase and 500 ml of upper phase were put into a separate reservoir and specific amount of methylene blue (MB) was added to the solvent system, mixed again and equilibrated at 25 °C until use. MB has a high extinction for the LED illumination wavelength used and is mostly soluble in the water rich lower phases that were used as mobile phases. For the measurement of viscosities and densities no dye was added to the solvent systems. The measurement of the interfacial tension was performed with and without MB.

2.3.2. Measurement of physical properties

The viscosities of both phases of every solvent system were measured with a capillary viscosimeter (type: capillary 0c, Schott Instruments). The viscometer was equilibrated at 25 °C and each phase was measured four times. The viscosities of each phase are given in Table 1. The standard deviations of the lower phases were from 0.2% to 1.1% (upper phases from 0.3% to 2%).

The density of every phase was measured using a density meter with oscillating U-tube (type: DMA 45, ANTON PAAR). The density meter was also equilibrated at 25 °C for all measurements and each system was measured four times. All densities and resulting density differences are shown in Table 1. The standard deviations of all phases were below 2%.

The measurement of interfacial tension was performed with a digital tensiometer (type: K10ST, KRUESS GmbH) with an accuracy of 0.1 mN/m and the Du Nouy ring method at 25 °C. All experiments were performed three times for two different solvent system preparations and each phase system. The standard deviation of each phase system was calculated from 6 experiments. Additionally the experiments were done with MB (overall concentration of 60 mg/l). We found no significant influence of MB on the interfacial tension. The difference was always within the standard deviation and the tensiometer accuracy. Therefore we used the averaged values of the six experiments without MB that are given in Table 1. The standard deviations of all experiments without MB were below 3%.

2.3.3. Preliminary experiments and one-phase calibration

First the optimal concentration of MB for a specific LED illumination time had to be found. A good compromise between low blurring (short illumination time), high contrast (high dye concentration and long illumination) and a high signal-to-noise ratio of the CCD sensor (long illumination time and high dye concentration) was found for an illumination time of 5 μs and a MB concentration of 30 mg/l in the mobile phase. This concentration still enabled the differentiation of the rotor (metal surface – complete light extinction) and parts of the chamber that only contained mobile phase (outlet of the chamber).

For image processing and calculation a preliminary calibration with water was performed. The rotor was filled with clear water and about 100 images were taken at a rotational speed of 1000 rev/min and a low flow rate of 5 ml/min. Then 150 ml water with a known MB concentration was pumped through the rotor at different volume flows and rotational speeds to replace the clear water. Again 100 images were taken for the flow rate of 5 ml/min. This procedure was repeated for 21 different concentrations of MB up to 30 mg/l. The calculation procedure for the calibration videos is shown in Section 3.2.1.

2.3.4. Photometric measurements

Additionally we measured the MB extinction with a photometer (SPECORD 50, Analytik Jena AG) at 623, 630 and 637 nm for different concentrations and path length of cuvettes. Before a sample with MB was measured a reference measurement without MB (clear fluid in the cuvette) was performed and its extinction was automatically subtracted from all following measurements. The cuvettes used were glass (1 mm, 2 mm and 5 mm path length) and

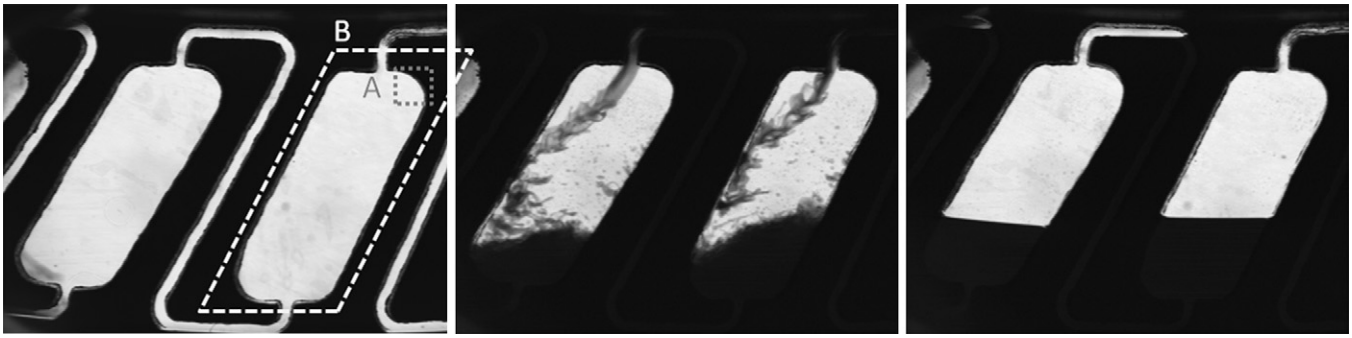

Fig. 4. Different types of video recorded: blank video (left), flow video (center) and retention video (right). A reference image section (A) and chamber polygon boundaries (B) in the blank video.

PMMA cuvettes with 10 mm path length (VWR international). For a concentration of 30 mg/l in the lower phase the MB concentrations of the stationary phases were measured. The most polar EtAcWat system showed a maximum MB concentration of 0.05 mg/l that equals a partition coefficient of 0.00167. The concentrations in the other stationary phases were significantly lower. Additionally the wavelength had only little influence. The results of the measured extinction and the resulting extinction coefficients ε_λ as a function of the MB concentration in the mobile phase are shown in Section 3.2.2. The results proved our assumption that the concentration of MB in the stationary phases can be neglected.

2.3.5. Flow visualization

Before each experiment the storage solution (ethanol/water – 1:1) had to be removed completely. Therefore 150–200 ml of the clear upper phase was pumped in descending mode direction through the rotor at varying rotational speeds between 200 and 1000 rev/min and high volume flows above 20 ml/min and collected in the waste tank. This procedure was derived from the behavior of the storage solution in the chambers and ducts. For low rotational speeds droplets of the storage solution stuck to the walls in the chambers and were not flushed out of the rotor. At higher rotational speeds most of these droplets were removed from the walls and were flushed out. But the rotational speed had to be lowered several times during the filling procedure because droplets of the storage solution stayed at the rotation axis outer side of the ducts. By lowering centrifugal acceleration these droplets were entrained by the flow into the next chamber. As long as the droplets did not stick again to a wall they kept moving towards the rotor outlet. After filling the rotor completely with stationary phase the flow was recycled into the reservoir.

Then three types of videos were recorded (see Fig. 4). First the so-called blank videos of the clear stationary phase were taken for each rotational speed. Therefore the delay time of the lighting controller was adjusted for every rotational speed in order to visualize always the same chambers of the rotor. When the delay times were identified the rotational speed was increased to 1800 rev/min to remove all remaining droplets of the storage solution from the chamber walls. Videos with approximately 100 images were recorded for each rotational speed investigated for a low stationary phase volume flow of 5 ml/min.

Thereafter the so-called flow videos in hydrodynamic equilibrium were recorded for each volume flow and rotational speed investigated. For switching between upper or lower phase of the solvent system a 3-port valve between reservoir and pump was used. Approximately one–three rotor volumes of mobile phase were pumped through the rotor until no stationary phase left the rotor and the signal of the UV-detector was constant. For the unstable phase systems or high volume flows always a small amount of stationary phase left the rotor. The change in the stationary phase retention could not be seen in the images but the signal of the UV-detector did not become constant for more than 20 s. This proved for some operating conditions stationary phase still left the rotor. If this so-called bleeding occurred, the measurement was started after five rotor volumes of mobile phase were pumped into the rotor.

The experiments were performed for a fixed volume flow and decreasing rotational speed. Videos of 300–500 images were taken for ten different rotational speeds between 1800 and 600 rev/min. After recording the last video for the slowest rotational speed the rotor was filled again with stationary phase before the next volume flow was measured. Volume flows of 3–30 ml/min were measured in steps of 3 ml/min.

After each flow video a so-called retention video (see Fig. 4 right) was recorded. Therefore the pumping was stopped so the mobile lower phase coalesced on the outer side of the rotor. Then a retention video of approximately 50 images was recorded before the pump was started again. In order to disturb the flow as little as possible, the volume flow was changed first, then the pump was started and finally the rotational speed was lowered. Preliminary experiments proved that the stationary phase retention was not lowered by this procedure.

3. Image processing and calculation

In this section the image processing routine and the calculation of different parameters is presented. The flow chart of the implemented program sequence is shown in Fig. 5. The software tool used is the open source image processing tool ImageJ [18]. Most parts were written in the ImageJ macro language provided. However the calculation of the mobile phase thickness and the interfacial area were excluded and written in Java plugins that provided a much faster processing.

3.1. Pre-processing

About 10% of all images were shifted 1–10 pixels compared to the position of the other 90%. In order to compare the position of each image a reference image section A (see Fig. 4) was used. From this particular section of 65 × 65 pixels the edge of the chamber was marked by using two ImageJ functions (max. entropy threshold, mark edges). This edge was compared to the edges of the other images of the video and the complete image was deleted if the edge was shifted in comparison with the majority of images.

The same image section was used to delete too bright or too dark images. Therefore the maximum grey value of each image in this section was identified and the most frequent value was marked. All images with a difference of more than one grey value to the most frequent value were deleted. The remaining images were saved as an image sequence (flow video) or averaged and saved as a single

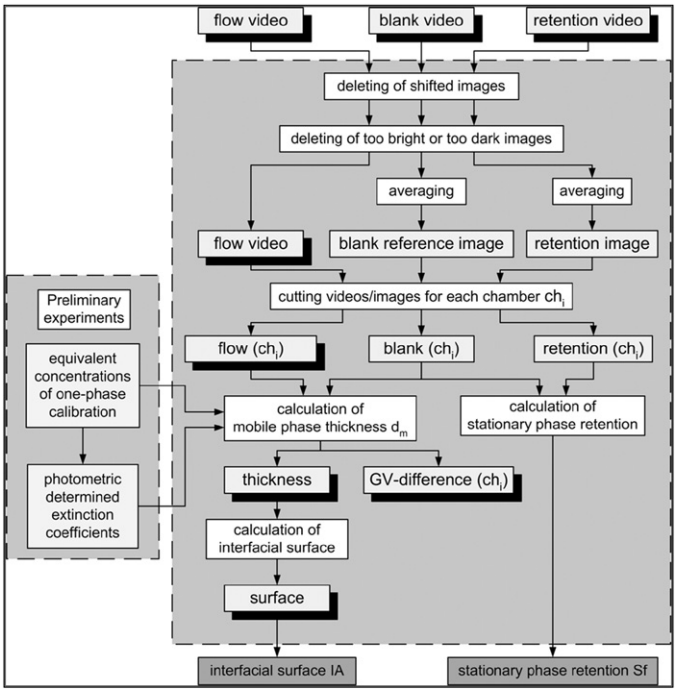

Fig. 5. Program sequence of the implemented image processing routine in ImageJ.

image (blank reference image, retention image). On each image four chambers were visible. The position of each chamber was marked by a polynomial (see Fig. 4) and was cut-out to allow independent analysis of each chamber.

3.2. Calculation of mobile phase thickness

Given that the blank reference image and each image of the flow video showed the same part of the rotor the difference in grey value ΔGV of each pixel (x/y) was calculated by:

$$\Delta GV_{xy} = GV_{blank,xy} - GV_{flow,xy} \quad (1)$$

In order to derive a relationship between differences in grey value ΔGV and the mobile phase thickness, following assumptions were made:

- extinction of the fluids in the chamber is only caused by the dye methylene blue (MB)
- light scattering at the interfacial surface can be neglected
- light extinction of the stationary phase can be neglected (MB concentration is zero – see Section 2.3.4)
- the ratio of extinction coefficients of the maximal concentration c_{max} = 30 mg/l and an arbitrary concentration c_i is independent of wavelength and penetrated thickness of mobile phase (see Section 3.2.2)

Then the light extinction E_λ is given by:

$$E_\lambda = lg\left(\frac{I_0}{I_1}\right) = \varepsilon_\lambda(c_m) \cdot c_m \cdot d_m + E_0 \quad (2)$$

where I_0 is the light intensity of the LED, I_1 is the resulting intensity, d_m is the penetrated thickness of the mobile phase, c_m is the MB concentration and ε_λ is the extinction coefficient as a function of c_m. E_0 is an unknown extinction that is caused by light absorbance, scattering and reflectance of FEP-foils and glass plates.

The extinction can also be expressed by the ratio of grey values of the clear stationary phase $GV_{c=0}$ and the grey value $GV_{d=d_m}$ of an arbitrary mobile phase thickness

$$E_\lambda = \frac{GV_{c=0}}{GV_{d=d_m}} \cdot f_1 \quad (3)$$

where f_1 is an unknown function that depends on the camera sensor, $GV_{c=0}$ and $GV_{d=d_m}$. The extinction for the LED wavelength(s) of the one-phase calibration (see Section 2.3.3) is given by

$$E_\lambda = \varepsilon_\lambda(c_i) \cdot c_i \cdot d_{max} + E_0 = \frac{GV_{c=0}}{GV_{c=c_i}} \cdot f_2 \quad (4)$$

where c_i is an equivalent concentration, d_{max} is the rotor thickness of 2.5 mm, $GV_{c=0}$ is the grey value of the calibration image without dye and $GV_{c=c_i}$ the grey value for the concentration c_i. On the assumption that f is independent of the position of the camera sensor and the constraint that $GV_{d=d_m} = GV_{c=c_i}$ follows that f_1 is equal to f_2. Equalizing Eqs. (3) and (4), subtracting E_0 and solving for d_m gives the desired relationship for the mobile phase thickness.

$$d_m = \frac{\varepsilon_\lambda(c_i)}{\varepsilon_\lambda(c_m)} \cdot \frac{c_i}{c_m} \cdot d_{max} \quad (5)$$

The calculation of the extinction coefficients ε_λ of the concentrations c_i and c_m is discussed in Section 3.2.2. The only unknown variable in Eq. (5) is the equivalent concentration c_i.

3.2.1. Calculation of equivalent concentrations from the calibration

The experiment of the one-phase calibration was done by the procedure given in Section 2.3.3. It allows the equivalent concentration c_i for a given pair of grey values $GV_{c=0}$ and $GV_{c=c_i}$ to be calculated. First the displaced and different illuminated images were deleted for every 22 recorded videos analogous to the procedure for the blank videos. Then the remaining images of each video were averaged and strung together. The new image sequence contained 22 images. The first image has a methylene blue (MB) concentration of zero and the last one a concentration of 30 mg/l. Then the grey values outside the chambers were manually set to 255 and a rectangle for each chamber was defined with 4 points in order to calibrate each chamber independently. This allowed examining the influence of the chamber location in the image because the chambers on the left and the right were always less illuminated than the two chambers in the image center. However, the results showed no influence of the chamber position on the correlation functions that were derived from each chamber.

In order to correlate grey value to the known concentrations c_{cal} of the calibration images a polynomial function was used. The following subroutine was implemented in ImageJ and executed for every grey value $GV_{c=0}$ between 100 and 254 (this routine was performed 155 times for each chamber):

- counting the number n of grey values $GV_{c=0}$ in the first image (MB concentration is zero) and buffering their coordinates (x/y) in the image
- reading-out of grey values of the remaining 21 images at the same coordinates (x/y) and buffering these values in 21 arrays with the length n
- dismissing $n/4$ of the lowest and highest grey values from each array
- averaging the remaining values to get a GV_{mean} value for each of the 21 arrays (=images)
- subtraction of the mean values GV_{mean} of each image from the actual $GV_{c=0}$ gives ΔGV_{mean}
- creating a new array with the ΔGV_{mean} values of each image (array has 22 values-21 images plus the first image with a ΔGV_{mean} of zero)

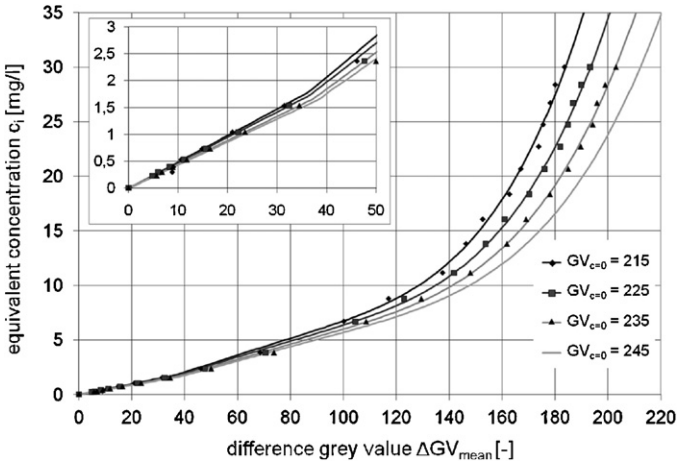

Fig. 6. Polynomial fit functions for different $GV_{c=0}$; values of $GV_{c=0} > 238$ were extrapolated (maximum in one-phase calibration). Image section shows detailed view on straight line fit and intersection point with polynomial fit.

- execution of a polynomial fit of forth degree ($\vec{x} = \Delta GV_{mean}$ array and $\vec{y} = \vec{c}_{cal}$)
- additional straight line fit for ΔGV_{mean} values with MB concentrations c_{cal} below 1 mg/l

If all $GV_{c=0}$ from 100 to 254 exist, 310 fit functions (155 polynomial, 155 straight line) were created and used to calculate equivalent concentrations c_i for each ΔGV and each $GV_{c=0}$. Some resulting fit functions for different $GV_{c=0}$ are shown in Fig. 6. For small values of ΔGV the straight line fit was used for the calculation because the polynomial of forth degree could not describe this section properly. From the intersection of both graphs the polynomial fit was used to calculate the equivalent concentrations c_i. The equivalent concentrations c_i were saved in a text file. From this file the equivalent concentration c_i for each grey value pair at the same pixel position (x/y) in a flow image $GV_{flow,xy}$ and the blank reference image $GV_{blank,xy}$ could be read-out in the program sequence (see Fig. 5).

3.2.2. Calculation of extinction coefficients

For extinction coefficients of the photometric measurements follows from Eq. (2)

$$\varepsilon_\lambda(c_i) = \frac{E_\lambda - E_0}{d \cdot c_i} \quad (6)$$

where d is the cuvette path length, c_i is the MB concentration, E_λ is the extinction and E_0 is zero because the reference measurement was subtracted automatically (see Section 2.3.4). The results of the serial dilutions and the regression functions of the form $E_\lambda = a \cdot c_i^2 + b \cdot c_i$ are shown in Fig. 7 for three different cuvette path lengths. By substituting the regression function of E_λ in Eq. (6) we get:

$$\varepsilon_\lambda(c_i) = \frac{a \cdot c_i + b}{d} \quad (7)$$

The calculated extinction coefficients ε_λ from this equation are shown in Fig. 8 for the different cuvettes. Given that only the ratio of extinction coefficients is needed for the calculation of the mobile phase thickness d_m in Eq. (5) the error is within 1% for different cuvette path length although the absolute difference is much higher. In the ImageJ routine the linear graph of the cuvette path length of 2 mm and a wavelength of 630 mm was used to calculate the extinction coefficients in Eq. (7).

As all values of Eq. (5) were known the mobile phase thickness d_m could be calculated. Thicknesses above the rotor thickness were limited to 2.5 mm and values below the pixel size of 25 μm were set to zero. Otherwise noise signals would be counted as mobile phase.

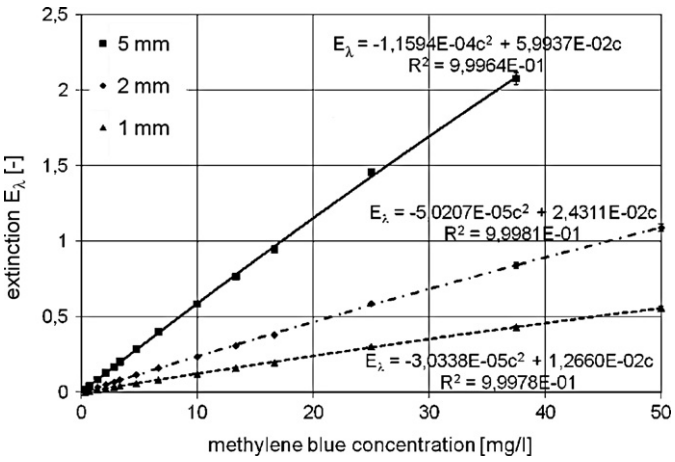

Fig. 7. Photometrical determined extinction of methylene blue and the regression functions from serial dilutions for different cuvette path lengths and a wavelength of 630 nm.

All calculated values were stored in so called thickness videos that were used for further calculations of droplet distribution profiles (see Section 4).

3.2.3. Treatment of "edge pixels"

Thicknesses of pixels at the edge of the chambers could not be reconstructed properly. One reason was that some light did not reach the sensor on the direct path because reflections from the sides of the chambers were detected. Additionally the rotation of the rotor led to blurring. So the light reached the sensor on the direct way only for a part of the illumination time. Therefore all edge pixels were neglected and received the mobile phase thickness of zero. The boundaries were set by analyzing the image manually. All grey values $GV_{c=0}$ of the blank reference images within the chambers were always above 100 and the grey values of pixels outside the chamber (metal) were always below 25. So a pixel was identified as an "edge pixel" if the grey value was between 25 and 100.

3.3. Calculation of stationary phase retention

The stationary phase retention Sf in CPC is defined as the ratio of stationary phase volume V_s and rotor volume $V_{rot} = V_s + V_m$. For the calculation the original blank reference and retention image were made binary (ImageJ function: max. entropy threshold) as shown in Fig. 9. The number of black pixels in the blank image $N_{s,blank,ch}$ and the retention image $N_{s,retention,ch}$ were counted and their numbers are proportional to the volume that was occupied by the stationary phase. The number of pixels in the duct $N_{s,blank,duct}$,

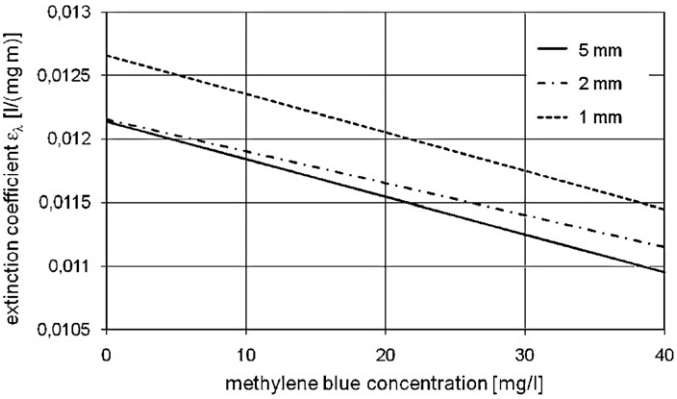

Fig. 8. Calculated extinction coefficients derived by the regression functions from Fig.ure 7 after Eq. (7).

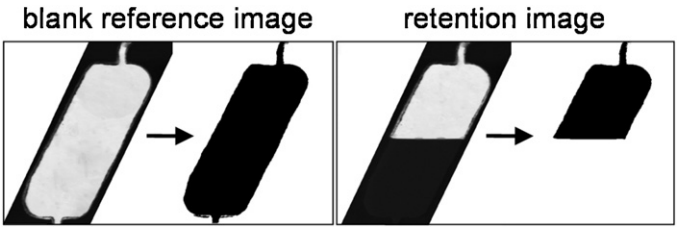

Fig. 9. Thresholding of blank reference image and retention image for the calculation of stationary phase retention.

which was not contained in the chamber images any more, was counted preliminary for different blank images. The rotor volume is proportional to the sum of $N_{s,blank,ch}$ and $N_{s,blank,duct}$. The retention videos were recorded after the pump was stopped. This caused the heavy mobile phase to leave the part of the duct that was close to the rotation axis. This was regarded by counting the number of pixels in the duct $N_{s,retention,duct}$ manually that were occupied by the stationary phase in different chamber retention images. The stationary phase retention was calculated by

$$\mathrm{Sf} = \frac{N_{s,retention,ch} + N_{s,retention,duct}}{N_{s,blank,ch} + N_{s,blank,duct}} \tag{8}$$

In the equation the values of $N_{s,blank,duct}$ and $N_{s,retention,duct}$ were set constant. The exemplary comparison of the stationary phase retention calculated from mobile phase thicknesses of the flow videos showed only small differences. The values for Sf from (8) were slightly higher because in the flow v the mobile phase at the wall was not detected completely due to the edge treatment criterion.

3.4. Calculation of interfacial area

From the values of the mobile phase thickness the interfacial area for mass transport was calculated. Given that only a 2D projection of the mobile phase thickness for each pixel existed, following assumptions had to be made:

- the jet, sheet or droplet of the mobile phase has a symmetry axis in the *xy*-plane
- there is only one droplet in the *z*-direction (no overlapping)
- the quadratic pixels have same size in the whole image (edge length $s = 25\ \mu m$)

The interfacial area between both phases can be calculated for each pixel by vector products. Therefore we assume a center pixel P_0 with the mobile phase thickness $d_{m,0}$ that is surrounded by 4 pixels with $d_{m,i}$ (above, left, below, right) as shown in Fig. 10. The resulting four vectors $\vec{S}_i$ for the pixel edge size s are:

$$\vec{S}_1 = \begin{pmatrix} 0 \\ s \\ \Delta d^*_{m,1} \end{pmatrix}, \quad \vec{S}_2 = \begin{pmatrix} -s \\ 0 \\ \Delta d^*_{m,2} \end{pmatrix}, \quad \vec{S}_3 = \begin{pmatrix} 0 \\ -s \\ \Delta d^*_{m,3} \end{pmatrix},$$

$$\vec{S}_4 = \begin{pmatrix} s \\ 0 \\ \Delta d^*_{m,4} \end{pmatrix} \tag{9}$$

Therein the differences of mobile phase thicknesses are given by $\Delta d^*_{m,i} = d_{m,i} - d_{m,0}/2$. The division by two is done due to the assumption of a symmetry axis in the *xy*-plane. The modulus of the vector product $\left|\vec{S}_i \times \vec{S}_j\right|$ equals the area of the parallelogram that is defined by the two vectors. For each pixel four vector products are calculated and therefore only one fourth of each parallelogram area belongs to the center pixel. The interfacial area of the pixel P_0

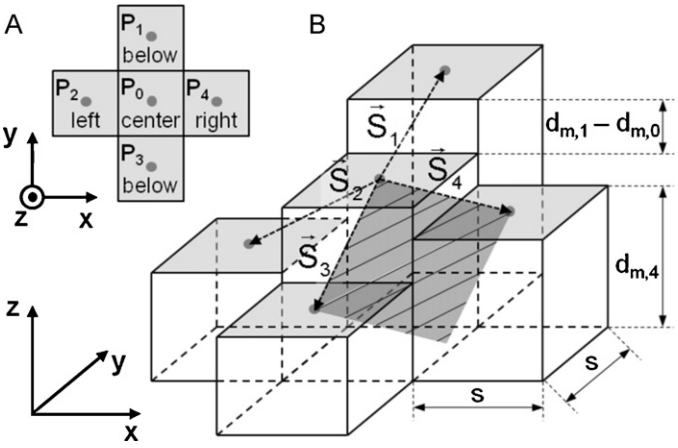

Fig. 10. Center pixel P_0 and neighboring pixels P_1, P_2, P_3 and P_4 in top view (A) and in 3D view with vectors, dimensions and one parallelogram area (B) for the calculation of the interfacial area.

can be calculated by

$$A_{P_0} = \frac{\left|\vec{S}_1 \times \vec{S}_2\right| + \left|\vec{S}_2 \times \vec{S}_3\right| + \left|\vec{S}_3 \times \vec{S}_4\right| + \left|\vec{S}_4 \times \vec{S}_1\right|}{4} \cdot 2 \tag{10}$$

The multiplication with two derives from the assumption of a symmetry axis in the *xy*-plane. Additionally three constraints for the vector products in Eq. (10) were defined:

$$\vec{S}_i \times \vec{S}_j = 0, \quad \begin{cases} (d_{m,i} - d_{m,0} = 0 \wedge d_{m,j} - d_{m,0} = 0) \vee (d_{m,0} = 0 \wedge d_{m,0} = d_{max}) \\ GV_{c=0}(d_{m,i}) < 100 \\ GV_{c=0}(d_{m,j}) < 100 \end{cases} \tag{11}$$

The topmost constraint sets the vector product to zero if only mobile phase ($d_{m,0} = d_{max}$) or only stationary phase ($d_{m,0} = 0$) is present in the center and the neighboring pixels. The second and third constraint ensured that all vector products with "edge pixels" were neglected and the interfacial area of "edge pixels" was set to zero. The calculation of the interfacial area was done for each pixel in the whole image and the sum equals the total interfacial area IA in the chamber.

4. Results and discussion

4.1. Flow analysis

For all solvent systems a strong deflection of the mobile phase was observed due to the Coriolis force. But the solvent systems investigated showed totally different hydrodynamic behavior. The flow pattern was strongly dependent on volume flow and rotational speed but also on the physical properties (densities, interfacial tension, viscosities). In Fig. 11 the different flow regimes for the phase systems can be seen:

- unbroken sheet for low rotational speeds and low or medium volume flows
- oscillating sheet for medium rotational speeds and most volume flows
- atomization for easy dispersible phase systems and high rotational speeds and volume flows

The phase systems in Fig. 11 are ordered by the ratio of interfacial tension and density difference $\sigma/\Delta\rho$. For the lowest volume flow the EtAcWat system showed the unbroken jet or oscillating sheet regime with relatively big droplets. For other phase systems with lower values of $\sigma/\Delta\rho$ the dispersion of the mobile phase increased and smaller droplets were observed. Higher rotational speeds generally shortened the sheet of mobile phase and enhanced

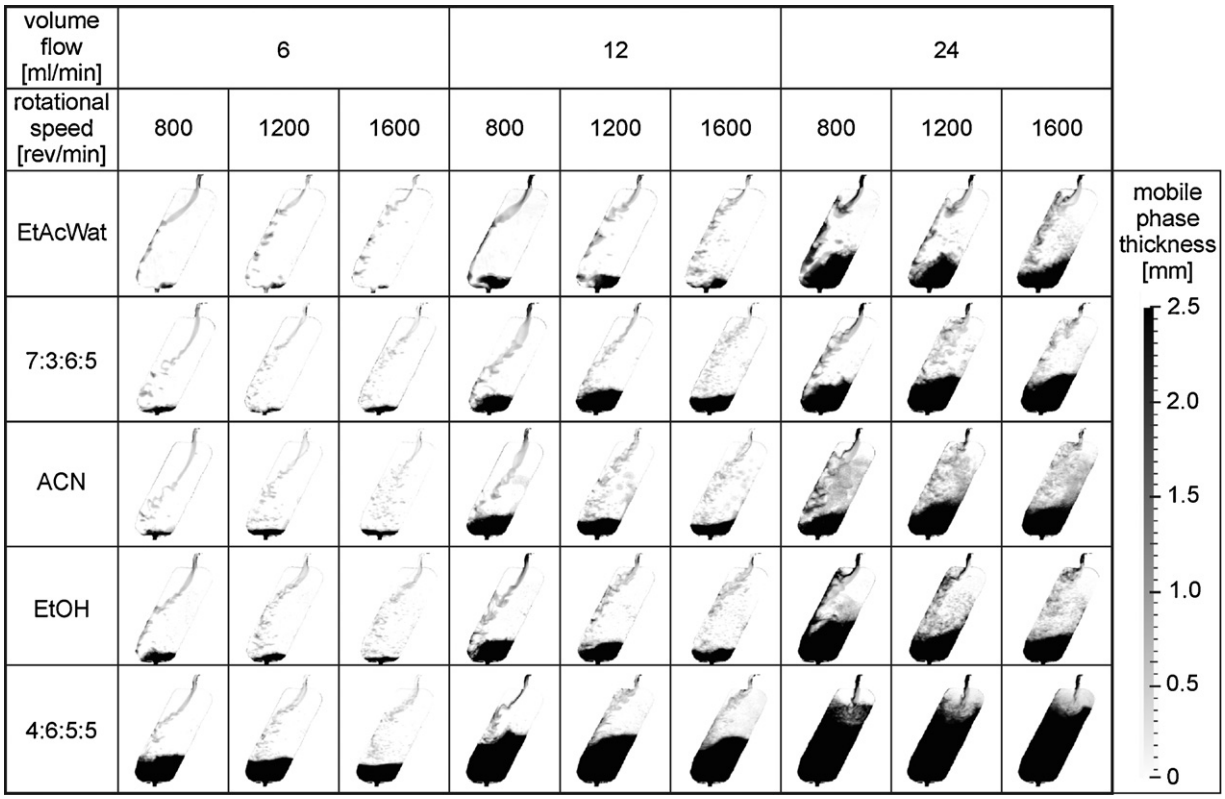

Fig. 11. Flow pattern and mobile phase thickness of solvent systems investigated for different volume flows and rotational speeds.

the formation of smaller droplets. The influence of the rotational speed on the stationary phase retention was small whereas higher volume flows also increased the dispersion but lowered the stationary phase retention strongly. For the 4:6:5:5 system nearly a complete loss of stationary phase was observed for high volume flows. The low stationary phase retention indicates that this system is the least stable of the solvent systems investigated.

The sheet mobile phase is already accelerated in the duct before it enters the chamber, which is clearly indicated by the lower mobile phase thicknesses in the ducts in Fig. 11. The ACN system (highest $\Delta\rho$) was accelerated most and the EtAcWat system (lowest $\Delta\rho$) had the lowest entrance velocities. For the EtAcWat system low volume flows and high rotational speeds caused the mobile phase to enter the chamber from the left wall of the duct. This behavior decreased for systems with higher density differences and has to be considered if the inlet geometry is changed.

4.2. Stationary phase retention

As expected the EtAcWat is the most and the 4:6:5:5 is the least stable system due to the parameter $\sigma/\Delta\sigma$. The results of the stationary phase retention calculation for four phase systems are shown in Fig. 12. The retention of the ACN system was very similar to the 7:3:6:5 system and is not shown.

Generally the stationary phase retention is rather a function of the volume flow than the rotational speed. For all solvent systems the stationary phase retention decreased for higher volume flows because the residence time in a chamber depends on the height of mobile phase in the coalescence zone. The coalescence time itself is governed by the centrifugal force, the drop diameters and therefore by physical properties and operating parameters. Higher values of the parameter $\sigma/\Delta\sigma$ led to larger droplets that usually coalesce faster. Increasing the rotational speed or the centrifugal force respectively should result in better coalescence but it also lowers the droplet size. Given that the stationary phase retention or the coalescence time respectively did not change very much with rotational speed these two effects seem to cancel each other out.

The smaller stationary phase retention of some solvent systems for lower rotational speeds is explained by the flow pattern. For some conditions the mobile phase entered the coalescence zone as a sheet or big droplets (see Fig. 11: EtOH-24 ml/min–800 rev/min). Mobile phase that enters the coalescence zone with a high velocity enhances the entrainment of stationary phase into the bulk of mobile phase. This decreases the distance and the time of stationary phase to reach the chamber outlet and resulted in lower stationary phase retention. Generally, the conclusion of Foucault [4], to specify the stability of a phase system (stationary phase retention) by the parameter $\sigma/\Delta\sigma$, seems reasonable.

The high stability or high stationary phase retention respectively of the EtOH system cannot be explained by the parameter $\sigma/\Delta\rho$. Its density difference and interfacial tension is close to the phase system 4:6:5:5 but the stationary phase retention was more similar to the 7:3:6:5 and ACN systems. A possible reason might be the viscosity ratio. Grace [21] proved experimentally that in simple Couette shear flow of high viscosity Newtonian fluids the breakup of a droplet occurs when a critical capillary number Ca_{crit} ($a_{crit} = \eta_c \cdot r_d \cdot \dot{\gamma}/\sigma$) is reached. The value of Ca_{crit} is only determined by the viscosity ratio p ($p = \eta_d/\eta_c$). Therein η_d is the viscosity of the dispersed phase (here mobile) and η_c of the continuous one, r_d the droplet radius, $\dot{\gamma}$ the shear rate and σ the interfacial tension. From very small p values Ca_{crit} decreases until it reaches a minimum between $0.1 < p < 1$. For $p > 1$ the value of Ca_{crit} increases and for $p > 4$ breakup is totally prevented. This is only valid for simple Couette shear flow but might explain the higher stationary phase retention of the EtOH system that has a high viscosity ratio $p = 4.5$.

4.3. Interfacial area and droplet distribution profiles

The interfacial area IA was calculated quantitatively for all phase systems using the protocol given in Section 3.4. In Fig. 13 two

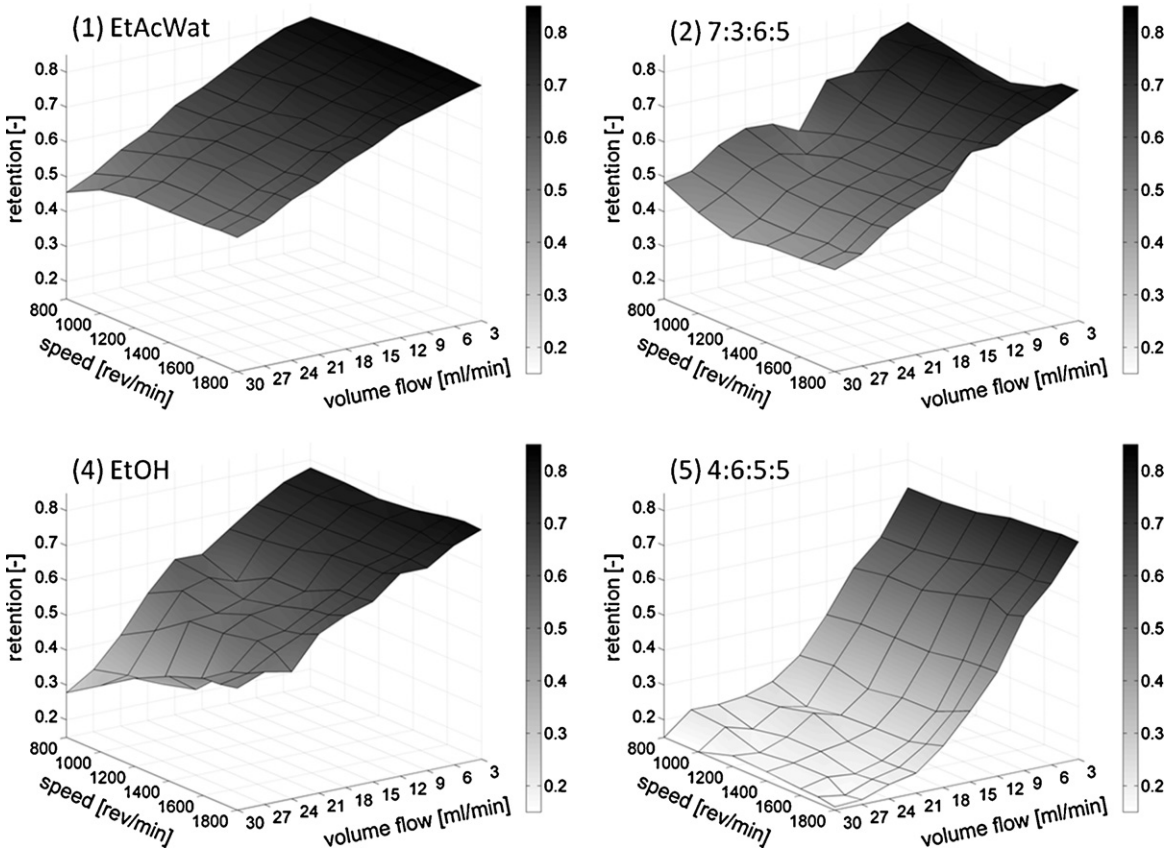

Fig. 12. 3D plots of stationary phase retention of solvent systems investigated for different volume flows and rotational speeds.

3D plots of the phase systems EtAcWat and EtOH are shown. The interfacial area was found to increase strongly with volume flow and only slightly with rotational speed. This was not expected but can be explained by the higher velocities of the mobile phase for higher rotational speeds. The interfacial area of a fixed volume would increase for smaller droplets. But a higher mean velocity of the mobile phase reduces the volume, which is in contact with the stationary phase. These two effects seem to compensate each other. But it has to be mentioned that the calculation of interfacial area is limited because for disperse flow patterns with overlapping droplets the interfacial area is underestimated. So the small influence of rotational speed on interfacial area is only correct for low and medium disperse flow patterns.

A maximum of the interfacial area was observed for different volume flows for all phase systems except the very stable EtAcWat system. The maxima were seen between 9 ml/min for the 4:6:5:5 and 18–21 ml/min for the 7:3:6:5, ACN and EtOH systems. These maxima indicate a reasonable limitation of the volume flow because the increase of interfacial area due to higher dispersion is compensated by decreasing retention. Nevertheless, the optimal operating parameters related to peak resolution would probably be found for lower volume flows because the interfacial area per volume of mobile phase in the chamber decreased for higher volume flows.

Several authors have shown that mass transfer is enhanced for increased rotational speed [4,7]. They assumed that the interfacial area increases for higher rotational speeds because of smaller droplets and more dispersed flows with smaller droplets. This behavior cannot be seen in the diagrams of the interfacial area in Fig. 13. Therefore we calculated mobile phase thickness distribution profiles. In these the pixel counts of each mobile phase thickness between 0.03 and 2.49 mm are shown. Thickness distribution profiles do not solve the problem of overlapping droplets in very disperse flows but give a better insight for the real droplet size distribution. Three small droplets that overlap in one pixel still give a mobile thickness that is much lower as in the sheet of the mobile phase.

For all phase systems the rotational speed has the same effect on the thickness distribution profiles in Fig. 14. Pixel counts of small mobile phase thicknesses are strongly enhanced whereas the pixel counts of high mobile phase thicknesses decreased with rotational speed. These results also correspond to the images in Fig. 11 where higher rotational speeds also lead to greater dispersion and smaller droplets. By comparison of the graphs in Fig. 14 with the flow pattern in Fig. 11 the graphs with high mobile thicknesses correspond to a mostly unbroken sheet that is most unfavorable for good mixing. The increase of pixel counts with rotational speed for values between 0.1 and 0.3 mm and decrease for values between 1.0 and 2.0 mm can explain higher separation efficiency due to better mass transfer of smaller droplets.

For the EtOH system a decrease of pixels with very small thicknesses below 0.1 mm was observed for 1600 rev/min. By examination of the image sequence we found droplets of mobile phase that were stuck to the wall. The tendency to wet to the surface of the FEP foil was lowered for higher rotational speeds due to higher centrifugal force but also for higher volume flows.

Besides the thickness of the mobile phase (droplet size) also the mobile phase volume that is in contact with the stationary phase has an influence on the mass transfer. The cumulative volume of dispersed mobile phase is the amount of mobile phase that is in contact with the stationary phase and not already coalesced ($d_m < 2.5$ mm). It was calculated by summing up the products of mobile phase thickness, pixel counts and the area of a pixel (625 μm^2). The cumulative volume of dispersed mobile phase is

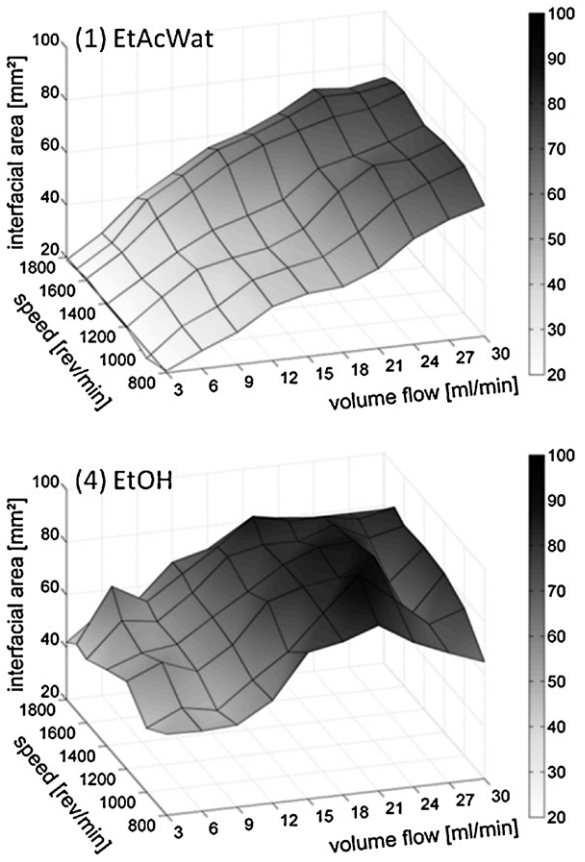

Fig. 13. 3D plots of interfacial area of EtAC and EtOH solvent system for different volume flows and rotational speeds.

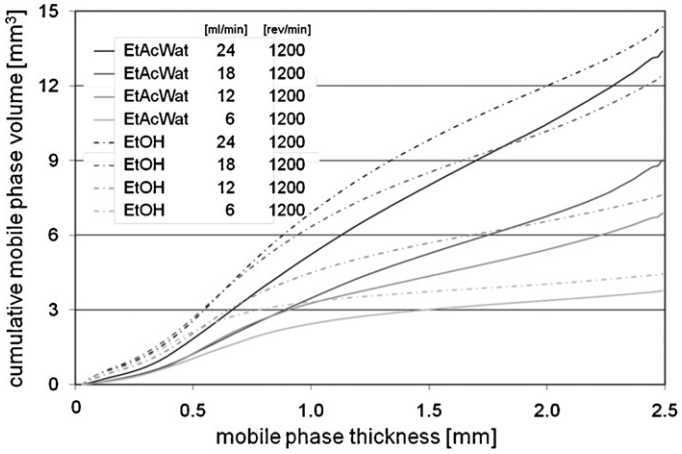

Fig. 15. Cumulative volume of mobile phase in the chamber that has a thickness between 0.03 and 2.49 mm (pixels with 2.5 mm were not taken into account because these were not in contact with the stationary phase), edge length of quadratic pixels was 0.025 mm

shown in Fig. 15. As expected the absolute volume for the EtOH system for the same volume flow is higher than for the more stable EtAcWat system. This results from lower velocities in the EtOH system because the droplet size is shifted towards smaller values.

For all systems an increase of cumulative volume of mobile phase above average was observed for specific operating parameters. This is shown for the EtOH system in Fig. 15 for the volume flows from 12 to 18 ml/min. This result is also confirmed by the image sequences that are shown in Fig. 16. Increasing the volume flow from 12 to 18 ml/min makes the flow pattern unsteady. For a volume flow of 12 ml/min the sheet of mobile phase oscillates but stays at the same position. For higher volume flow above 18 ml/min the sheet often changes the direction. This unsteady behavior leads to greater dispersion because the sheet breaks at different positions. For the more stable EtAcWat this increase of the absolute cumulative volume above average was seen for higher volume flows and especially higher rotational speeds.

Measurements of Marchal already proved that besides higher rotational speeds also higher volume flows can enhance the resolution of a separation [16]. The droplet distribution profiles in Fig. 14 and the cumulative volume of mobile phase in Fig. 15 can only partly explain this behavior. One reason for better resolution is the already mentioned unsteady flow with stronger sheet breakup that creates "new interfacial area". In a stable sheet of mobile phase mass transport limitations are expected from the inner part to the surface of the sheet. This results in a concentration profile of a solute in the sheet of mobile phase at the chamber entrance. If the sheet (or a big droplet) of mobile phase breaks up the solute concentration at the "new interface" jumps up and mass transfer between mobile and stationary phase is enhanced. The increasing diversity of flow and sheet breakup for increasing volume flows for the EtOH system is shown in Fig. 16 for 1200 rev/min. The flow pattern for 6 ml/min was relatively steady and the sheet breakup occurred in the middle of the chamber. Increasing volume flow decreased the

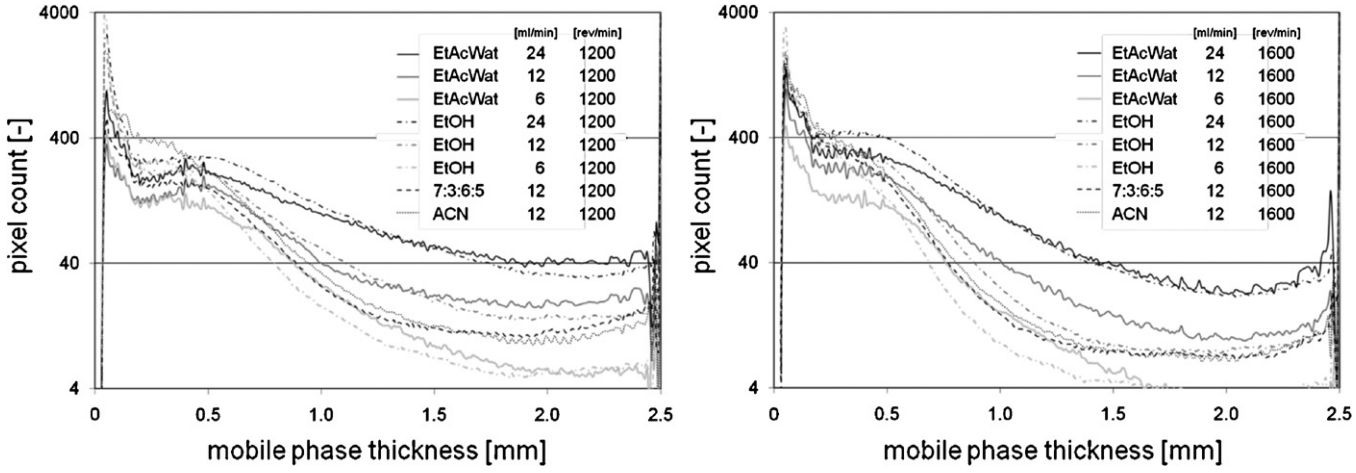

Fig. 14. Mobile phase thickness distribution profiles for videos from Fig. 11; minimum calculated value was 0.03 mm, maximum value was 2.49 mm (chamber depth), range for each pixel was 0.01 mm (this leads to 247 different values for mobile phase thickness).

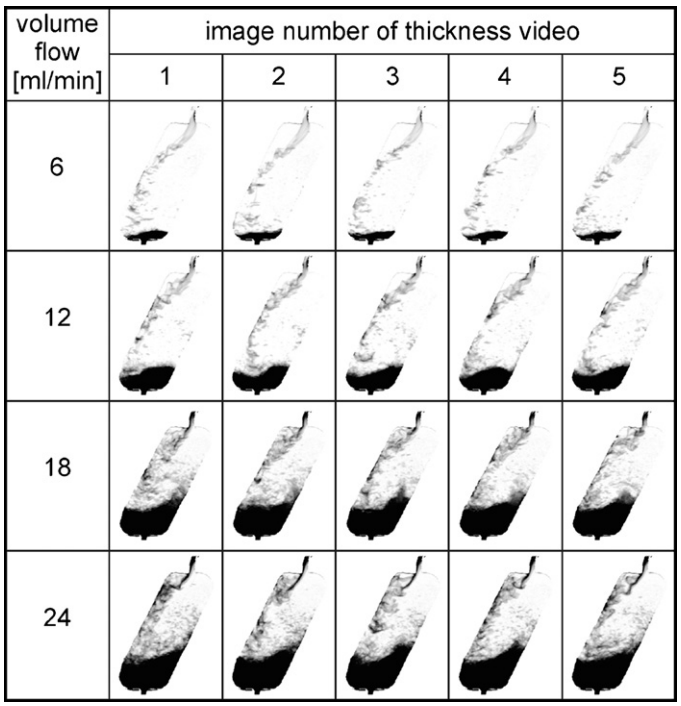

Fig. 16. Image sequences of mobile phase thicknesses of EtOH system for 1200 rev/min and different volume flows (for scale mobile phase thickness see Fig. 11).

length of the stable sheet and thus more "new interfacial area" was created.

Another probably more important reason might be the formation of dead zones in the chamber for relatively low volume flows. Large parts of the chamber are free of mobile phase and the convective transport in the stationary phase is also relatively small. If solutes are dissolved in the stationary phase it takes a very long time until it is in contact with the mobile phase again. However, many dead zones in a chamber are expected to cause strong peak broadening due to increased residence time distribution of the solutes. Like higher rotational speed also higher volume flows of the mobile phase increase the drag force on the stationary phase and its velocity. This enhances the convective transport in the stationary phase and leads to the unsteady sheet already mentioned.

Very high volume flows lower the stationary phase retention significantly especially if the mobile phase enters the coalescence zone with high velocities or as stable sheet. Therefore smaller droplets with lower velocities entering the coalescence zone are preferred. Additionally a sheet of mobile phase or large droplets that enter the coalescence zone lead to strong mixing of the already coalesced mobile phase (see Fig. 16). This results in strong backmixing of the mobile phase and increases peak broadening.

4.4. Effect of Coriolis force

The influence of Coriolis force and the resulting sheet deflection strongly depends on operating parameters and properties of the solvent system. For most flow patterns in Fig. 11 the Coriolis force deflects the mobile phase until it reaches the chamber wall, which reduces the interfacial area for mass transfer. Additionally the mobile phase at the wall is accelerated and enters the coalescence zone with high velocities. As already mentioned this behavior lowers stationary phase retention and increases backmixing of the mobile phase.

Generally the sheet deflection decreases with increasing density difference $\Delta\rho$ of a solvent system. Thus the sheet of the EtAcWat system was deflected most and that of the ACN system least. For a droplet of the lower phase in the analyzed descending mode with the mass m_d and the velocity $\vec{v}$ with a tangential and a radial component the ratio of centrifugal force F_{ce} and Coriolis force F_{Co} is given by

$$\frac{F_{ce}}{F_{Co}} = \frac{m_d \cdot \Delta\rho \cdot \omega^2 R - 2 \cdot m_d \cdot \rho_m \cdot v_{tan} \cdot \omega}{2 \cdot m_d \cdot \rho_m \cdot v_{rad} \cdot \omega} = \frac{\Delta\rho \cdot \omega \cdot R - 2 \cdot \rho_m \cdot v_{tan}}{2 \cdot \rho_m \cdot v_{rad}} \quad (12)$$

Therein R is the radial distance between rotation axis and droplet position and ω is the angular frequency. Eq. (12) clearly indicates that the influence of Coriolis force decreases with increasing density difference. Our calculations of the path of a single droplet with the simple model presented by Ikehata [22] gave the same result. But this model only takes centrifugal and Coriolis acceleration into account. The limitation of the velocity $\vec{v}$ as a function of drag, droplet size and shape and the properties was neglected. But the velocity of a droplet is limited and droplet break-up can occur if the drag force is increased. For more dispersed flows with smaller droplets the deflection should decrease because of lower velocities v_{tan} and v_{rad} in Eq. (12) and thus a smaller influence of the Coriolis force compared to the centrifugal force. This behavior was not observed in the experiments. Only for the lowest volume flow the sheet deflection decreased for higher rotational speeds and thus smaller droplets.

Generally the sheet deflection increased for higher volume flows and rotational speeds. This indicates an additional force that acts on the sheet of mobile phase. The stronger sheet deflection is probably the result of a circulating flow of stationary phase on the right side of the chamber that deflects the sheet stronger than the Coriolis force would do alone. The increase of volume flow and rotational speed enhances the drag force on the stationary phase due to the higher momentum of the mobile phase. The higher circulation velocity of the stationary phase causes a stronger sheet deflection of the mobile phase. This behavior was observed for all solvent systems. One exception was seen for the 4:6:5:5 system. The sheet deflection vanished for a very low stationary phase retention (see Fig. 11). The sheet or the droplets were barely deflected at all and entered the coalescence zone in the center. The short distance between chamber entrance and coalescence zone and the high momentum exchange of the droplets most likely resulted in two circulating flows of stationary phase on either side of the sheet that kept it away from the walls.

In order to keep the sheet away from the chamber walls the ratio in Eq. (12) can be reduced by changing the rotor radius R. For a constant centrifugal acceleration in two different rotors with the radii R_1 and R_2 the product of ω and R in Eq. (12) increases by

$$\frac{\omega_2 \cdot R_2}{\omega_1 \cdot R_1} = \sqrt{\frac{R_2}{R_1}} \quad (13)$$

while all other parameters staying constant. Therefore CPC devices with greater rotor radii seem desirable especially for phase systems with low density differences because the influence of the Coriolis force is lowered.

5. Conclusions

In this study we presented a new setup for an optical measurement system for flow visualization in CPC that improved the quality of the images immensely. The improved contrast between the phases allowed the calculation of parameters like mobile phase thickness, its distribution and the interfacial area directly from the images for the first time.

By analyzing the flow pattern, retention, interfacial area, mobile phase thickness profiles and the mobile phase volume that is in contact with the stationary phase, we were able to explain the different separation efficiencies. Higher rotational speed generally enhanced dispersion and in most cases the stationary phase retention. But also higher volume flows were detected to cause better dispersion and additionally minimizing dead zones in the chamber.

The ratio of interfacial tension and density difference proved to be useful to estimate the stability of a biphasic system. But also the viscosity ratio was found to have an influence on the flow pattern. It has to be mentioned that this study was performed for five phase systems and in descending mode only. The authors are aware that all the results are restricted to descending mode although most pharmaceutical companies use ascending mode with the organic phase mobile. Finally only real separations can describe the relative effect of increasing interfacial area and decreasing stationary phase retention. Nevertheless, we demonstrated that the operating parameters should be chosen carefully with respect to physical properties.

The effect of the Coriolis force on the flow pattern was shown. Especially the mobile phase in low density difference solvent systems was deflected strongly because the resulting Coriolis acceleration is proportional to density and not to its difference like the resulting centrifugal acceleration. In order to reduce the effect of the Coriolis force the rotor radius can be increased.

We suggest that less stable solvent systems should be operated at low volume flows and medium rotational speeds. For medium stable it seems better to increase the volume flow than to increase the rotational speed. Very stable systems are not usable very well in CPC. The combination of volume flow and rotational speed that give good dispersion for very stable solvent systems (e.g. EtAcWat) cannot be reached because of pressure limitation of the rotary joints. The highest rotational speed and volume flow used in this study would have a twofold higher pressure drop in the semi-preparative rotor with 20 rotor plates than the 60 bar allowed. Nevertheless, a CPC system should be operated near the maximum pressure limit of the rotary joints.

Acknowledgements

Thanks to the financial support (Grant No. FKZ 0315404) from the federal ministry of education and research (BMBF) and the cluster of industrial biotechnology (CLIB2021). The authors also want to thank the workshop of the TU Dortmund for help with the construction of the transparent rotor and Thomas Pischel for his experimental work.

References

[1] W. Murayama, T. Kobayashi, Y. Kosuge, H. Yano, Y. Nunogaki, K. Nunogaki, J. Chromatogr. 239 (1982) 643.
[2] Y. Ito, M. Weinstein, I. Aoki, R. Harada, E. Kimura, K. Nunogaki, Nature 212 (1966) 985.
[3] J.B. Friesen, G.F. Pauli, J. Liquid Chromatogr. Related Technol. 28 (2005) 2777.
[4] A.P. Foucault, E.C. Frias, C.G. Bordier, F. Legoffic, J. Liquid Chromatogr. 17 (1994) 1.
[5] M.J. van Buel, F.E.D. van Halsema, L.A.M. van der Wielen, K.C.A.M. Luyben, AIChE J. 44 (1998) 1356.
[6] M.J. vanBuel, L.A.M. vanderWielen, K.C.A.M. Luyben, AIChE J. 43 (1997) 693.
[7] L. Marchal, A. Foucault, G. Patissier, J.M. Rosant, J. Legrand, J. Chromatogr. A 869 (2000) 339.
[8] F. de La Poype, R. de La Poype, P. Durand, A. Foucault, J. Legrand, G. Patissier, J.M. Rosant, US Patent 2003/6537452 B1, 2003.
[9] A. Foucault, J. Legrand, L. Marchal, D. Durand, US Patent 2008/003546 A1, 2008.
[10] A. Foucault, J. Legrand, L. Marchal, C. Elie, P. Agaise, US Patent 2010/0252503 A1, 2010.
[11] E. Delannay, A. Toribio, L. Boudesocque, J.M. Nuzillard, M. Zeches-Hanrot, E. Dardennes, G. Le Dour, J. Sapi, J.H. Renault, J. Chromatogr. A 1127 (2006) 45.
[12] F. Couillard, A. Foucault, A. Durand, US Patent 2006/0243665 A1, 2006.
[13] A. Berthod, M.J. Ruiz-Angel, S. Carda-Broch, Anal. Chem. 75 (2003) 5886.
[14] Y.B. Lu, Y.J. Pan, A. Berthod, J. Chromatogr. A 1189 (2008) 10.
[15] L. Marchal, O. Intes, A. Foucault, J. Legrand, J.M. Nuzillard, J.H. Renault, J. Chromatogr. A 1005 (2003) 51.
[16] L. Marchal, J. Legrand, A. Foucault, AIChE J. 48 (2002) 1692.
[17] A. Berthod, B. Billardello, J. Chromatogr. A 902 (2000) 323.
[18] W.S. Rasband, ImageJ, U.S. National Institutes of Health, Bethesda, MD, USA, http://rsb.info.nih.gov/ij/, 1997–2009.
[19] R. Margraff, in: A.P. Foucault (Ed.), Centrifugal Partition Chromatography, Chromatographic Science Series, Marcel Dekker, New York, 1994, p. pp. 331 (Chapter 12).
[20] Official Journal of the European Union L225, Commission Directive 2010/59/EU (2010).
[21] H.P. Grace, Chem. Eng. Commun. 14 (1982) 225.
[22] J.I. Ikehata, K. Shinomiya, K. Kobayashi, H. Ohshima, S. Kitanaka, Y. Ito, J. Chromatogr. A 1025 (2004) 169.